energies

MDPI

Article

Comparison of the 60Sn40Pb and 62Sn2Ag36Pb Solders for a PV Ribbon Joint in Photovoltaic Modules Using the Thermal Shock Test

Min-Soo Kang [1], Yu-Jae Jeon [2], Do-Seok Kim [1] and Young-Eui Shin [1,*]

[1] School of Mechanical Engineering, Chung-Ang University, Seoul 156-756, Korea; kang10101@cau.ac.kr (M.-S.K.); kdoseok@naver.com (D.-S.K.)

[2] Department of Automotive, Yeoju Institute of Technology, Gyeonggi-do 12652, Korea; superlittle@yit.ac.kr

* Correspondence: shinyoun@cau.ac.kr; Tel.: +82-2-820-5315

Academic Editor: Senthilarasu Sundaram

Received: 15 January 2017; Accepted: 10 April 2017; Published: 13 April 2017

Abstract: In this study, the characteristics of a photovoltaic (PV) ribbon (t = 0.25 mm) joint with 60Sn40Pb and 62Sn2Ag36Pb solders were evaluated using thermal shock tests. The thermal shock tests were performed under three conditions: −40–65 °C, −40–85 °C, and −40–105 °C. The results of these tests were analyzed using electroluminescence (EL) and cross-sectional images. Following testing, broken metal fingers (MFs) were confirmed near the solder joint. PV module degradation was attributed to the broken finger ratio (BFR) based on quantitative analysis of the dark rectangular (DR) regions on the EL images. In addition, the activation energy of the broken MFs was calculated from the increasing BFR. Thermal characteristic variations due to the added Ag in the PV ribbon solder joints were evaluated through observation of solder micro-structure changes following thermal shock tests.

Keywords: electroluminescence (EL); dark rectangular (DR); broken finger ratio (BFR); 60Sn40Pb (SP); 60Sn2Ag38Pb (SAP)

1. Introduction

To address energy depletion and environmental issues such as the instability of oil prices, depletion of fossil fuels, and the Fukushima nuclear power plant accident in Japan, more attention is being focused on renewable energy [1–3]. Among the many types of renewable energies, silicon solar cells have been the most common for industry use due to their low-price and machinability. Currently, more than 90% of annual solar cell production is based on crystalline silicon wafers, making silicon wafer-based technology the most important technology for photovoltaic modules (PV modules) [4]. Since the first silicon solar cell was reported in 1941, there have been substantial improvements in silicon cell performance, culminating in the 25.0% value reported in the present paper [5]. Many researchers have studied silicon-alternative materials and PV module reliability according to constraint properties such as the band-gap energy and efficiency limit.

Many manufacturers in the photovoltaic industry offer warranties of 20 years or longer for PV modules with incomplete knowledge of their reliability in the diverse environments in which these modules are typically deployed [6]. A number of researchers have studied the degradation characteristics of PV modules in real-time outdoor conditions. A study by Polverini showed that PV modules have an average efficiency degradation of 0.8%/year [7]. The National Renewable Energy Laboratory (NREL) research group presented measurements from individual modules and entire systems showing a mean degradation rate of 0.8%/year and a median value of 0.5%/year. In particular, 78% of all data reported a degradation rate of <1.0%/year [8]. Herrmann et al. [9]

reported that performance decreases due to light exposure over a span of three years using the standard IEC 61215. Degradation in PV modules is largely due to environmental factors such as temperature, humidity, discoloration resulting from ultraviolet (UV) exposure, and external forces. The PV ribbon solder joint is suspected to be the weakest point, based on typical PV ribbon solder joint problems such as cell cracks, inactive cracks, and broken metal fingers (MFs) caused by cycling heating. In addition, Jeon mentioned that the PV ribbon solder joint is the weakest point during thermal cycling, high-temperature, and humidity tests [1]. Yang et al. [10] performed aging tests for the growth of intermetallic compound layers (IMCs) at PV ribbon solder joints. These results demonstrated that two types of IMCs (Ag-Sn and Cu-Sn) were formed in the solder joints; since then, Sn-Pb solder alloys have been regulated according to RoHS (Restriction of Hazardous Substances), and lead-free solders are mandated throughout the industry. The use of lead-free solders leads to thermal and reliability problems due to their high melting points. The reliability tests for PV ribbon solder joints are necessary for producing high-reliability PV modules. Specifically, the damage to PV ribbon joints resulting from cyclic heat and high-temperatures must be analyzed. In this study, we analyzed broken metal fingers in coated 60Sn40Pb (SP) and 60Sn2Ag38Pb (SAP) solder PV ribbon joints using cyclic temperature (ΔT) over time (t). Further, we evaluated the variations in PV ribbon joint characteristics following the addition of silver (Ag) by analyzing images of broken MFs to determine the activation energy and metal structures.

2. Experiment

Images of various specimens are shown in Figure 1. The solar cell in this study was made using a 6-inch (238.95 cm^2) monocrystalline silicon wafer. MFs and 3-line electrodes were formed using an Ag paste sintering process on the silicon wafer. Ribboned cells were manufactured via a PV ribbon (60Sn40Pb and 60Sn2Ag38Pb) tabbing process (soldering process) at a temperature of 350 °C on the formed electrodes silicon wafer. To make the PV module, ribboned cells were used to perform a laminating process with exposure to a vacuum for 360 s, pressing for 30 s, and curing for 540 s at 150 °C. The glass thickness was 3.2 mm, the ethylene-vinyl acetate (EVA) thickness was 0.5 mm, the Poly-Vinyl Floride (PVF) type backsheet thickness was 0.3 mm, and the ribbon size was 0.25 mm (depth) by 1.5 mm (width). We manufactured 15 pieces of PV module specimens to determine the reproducibility of each solder type. The thermal shock test was performed to evaluate the changes in characteristics due to the added Ag in SP solder and SAP solder. The thermal shock test was performed under the three conditions shown in Table 1. The thermal shock test was performed for 700 cycles, where the cycles consisted of a high temperature (T_{max}) for 15 min followed by a low temperature (T_{min}) for 15 min. The temperature transfer time was 5 s for the elevator, and the temperature ramping time was less than 2 min. The specimens were prepared in groups of ten, one group for each solder composition and condition for the thermal shock test.

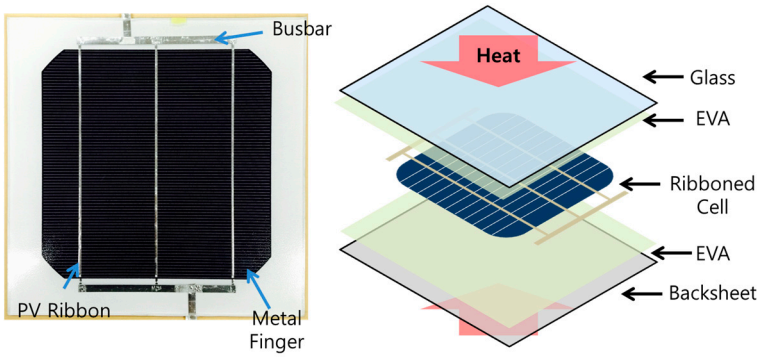

Figure 1. Structure of the photovoltaic (PV) modules.

Table 1. Temperature profile of the thermal shock test.

Test Conditions	T_{min} (°C)	T_{max} (°C)	Dwell time (min)	Cycle (min)
Condition 1 (Δ105)	−40	65		
Condition 2 (Δ125)	−40	85	15	1/30
Condition 3 (Δ145)	−40	105		

We obtained electroluminescence (EL) images to verify the changes in characteristics of the PV module according to the thermal shock test. In contrast to images obtained by detecting infrared radiation caused by thermal effects, a luminescence image is obtained from photons emitted by the recombination of excited carriers into a solar cell [11]. This excitation can be achieved by means of an injected current, which induces an EL effect [12]. Process deficiencies such as small cracks, breaks, and finger interruptions appear as dark rectangular (DRs) in the EL image [13]. In general, the broken MFs occurred near the ribbon joints, as shown in Figure 2, when the PV ribbon joints were subjected to thermal stress. The broken MFs formed DRs in the EL image, as shown in Figure 3. We calculated the broken finger ratio (BFR) using Equation (1) in order to quantify the broken MFs associated with thermal cycling. The BFR equation was used to compare the EL images and the DR images. We determined the activation energy of the broken MFs based on the thermal shock test with increasing BFR.

$$Broken\ Finger\ Ratio(BFR) = \frac{Dark\ \ Rectangular\ (DR)}{Surface\ of\ PV\ module} \quad (1)$$

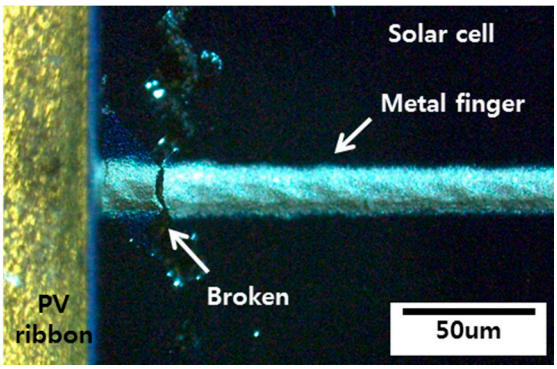

Figure 2. Disconnection of metal fingers (MFs).

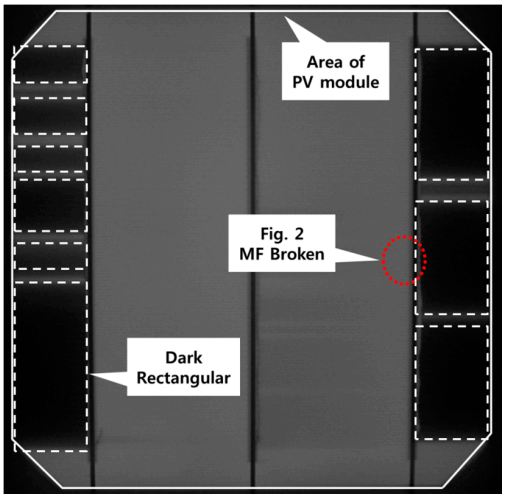

Figure 3. Dark rectangular regions in an electroluminescence (EL) image.

3. Results and Discussion

The broken MFs in the PV module were measured in a 100-cycle thermal shock test using EL images. Matevz stated that EL images show changes in crystalline silicon solar cells under many different circumstances, including broken fingers, oven effects, impact cracks, and inactive cracks [14,15]. In this study, two types of EL image changes are verified, as shown in Figure 4. The first occurs due to internal cracking of the cell. We confirmed the diagonal cracks in the EL image, as shown in Figure 4a. Such diagonal cracks are characteristic of monocrystalline silicon wafers and anisotropic materials [16]. However, the internal cracks are inactive and do not influence the efficiency or changes in the EL images. The second type of EL image change is DRs, as shown in Figure 4b. Chaturvedi et al. [17] stated that broken MFs cause DRs in EL images due to the electrical disconnection effect that occurs in EL images. Broken MFs obstruct photovoltaic effects by blocking the electric current, eventually influencing the PV module efficiency and decreasing the productive area.

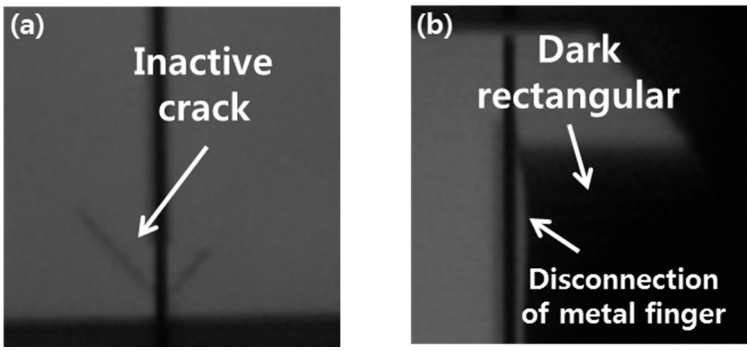

Figure 4. Defects of PV modules. (**a**) Inactive cracks; and (**b**) dark rectangular.

The EL image changes are shown in Figure 5 and are dependent on the thermal shock test and temperature conditions. A stain was observed in the EL images of the SAP solder PV ribbon joints at −40–105°C. This stain is due to impurities on the solar cell surface, which can occur if workers touch the solar cell surface with their bare hands or if the surface texturing of the solar cell is destroyed. We ignored this stain because it has no effect on the solar cell ribbon solder joints.

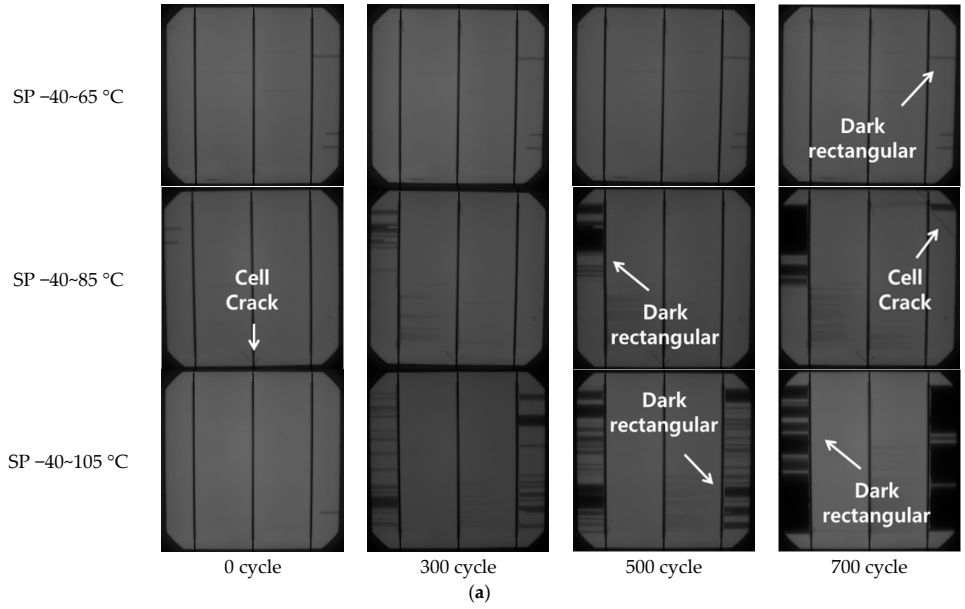

Figure 5. *Cont.*

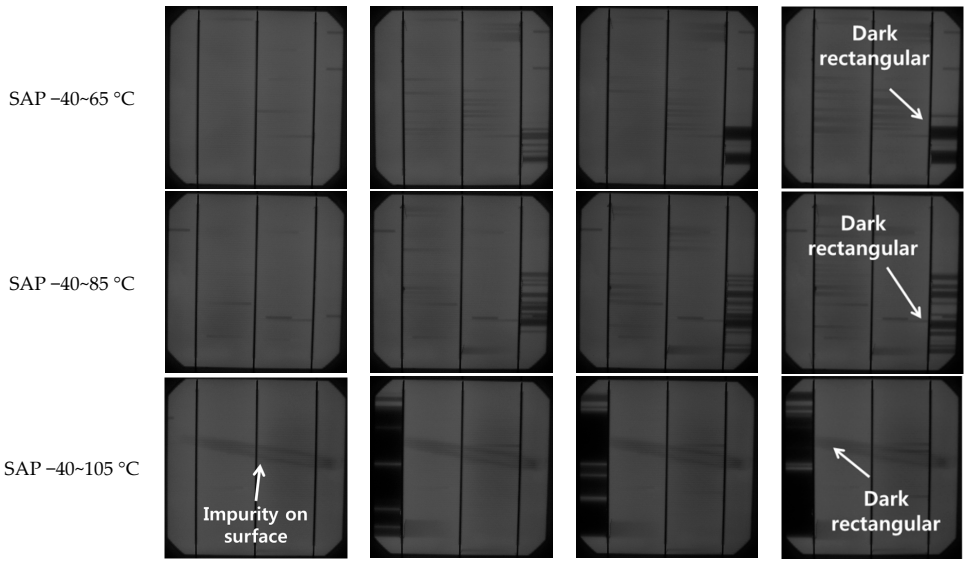

Figure 5. Changing of EL images: (**a**) EL images of the PV module using SP solder; and (**b**) EL images of the PV module using SAP solder.

After the test, the tendency of the DRs was checked with ten specimens following each solder composition and test condition, and it was observed that the DR tendency differed greatly according to solder composition. On the SP solder PV ribbon joints, the DR exhibits a gradually increasing tendency according to the number of test cycles. However, an increase in DR was not verified at the lowest temperature condition of −40–65 °C. For the SAP solder PV ribbon joints, an increasing DR was confirmed for all thermal shock test conditions. Based on these results, we calculated the BFR using Equation (1) according to the test conditions and test cycle accumulation, as shown in Figure 6.

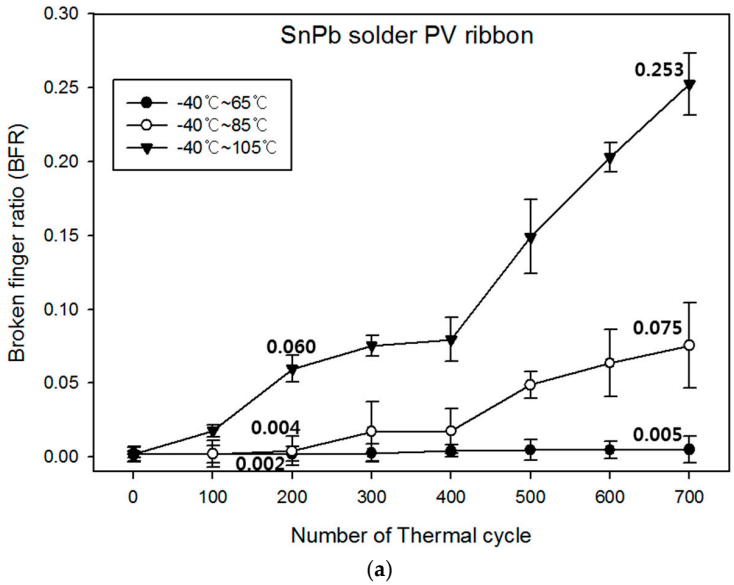

Figure 6. *Cont.*

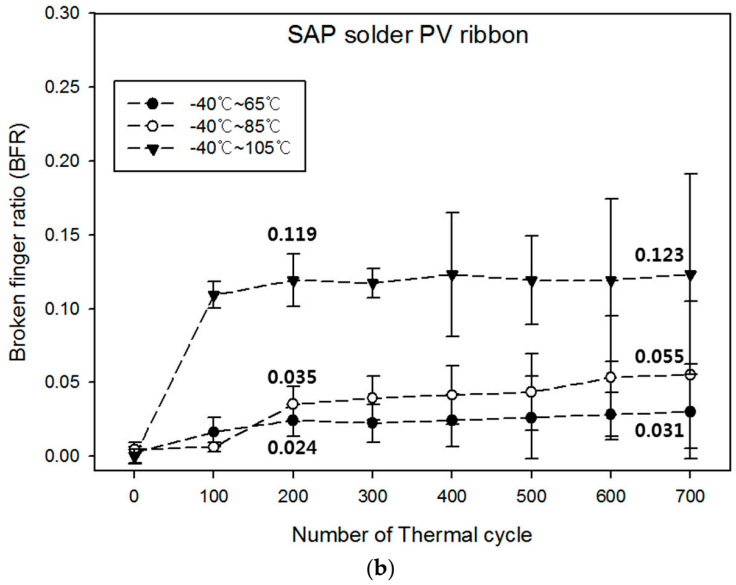

Figure 6. BFR growth in the solder: (**a**) BFR graph of the SP solder; and (**b**) BFR graph of SAP solder.

In the SP solder ribbon joints, the BFR stabilized in the range of −40–65 °C. However, in the harsh temperatures between −40 °C and 105 °C, the BFR increased to 0.253. On the other hand, the BFR exhibited increases under all test conditions for SAP solder ribbon joints. This increase in BFR became constant after 200 cycles.

These BFR values were measured from the broken MFs, and these broken MFs only appeared near the solar ribbon solder joints. It may be the case that degradation and metallurgical defects on solar ribbon solder joints influence the broken MFs. Thus, assessment of the broken MFs and BFR values are an appropriate foundation for the analysis of solar ribbon solder joint degradation. We calculated the activation energy of broken MFs on the solar cell surface using the calculated BFR, which increased as a function of time [18,19], as shown in Figure 6. The relationship between BFR (Y) and cycling-time (t) can be explained using Equation (2):

$$Y = Y_0 + \sqrt{Dt} \tag{2}$$

where Y_0 is the initial BFR at t = 0 and D is the BFR diffusion coefficient. When the BFR (Y) is plotted against the square root of the aging time ($t1/2$), the slope of the graph is equal to the square root of the diffusion coefficient ($D1/2$). The diffusion coefficient is a function of the temperature, as expressed by the Arrhenius in Equation (3):

$$D = D_0 e^{\frac{-Q}{RT}} \tag{3}$$

where D_0 is a temperature-independent constant known as the frequency factor, Q is the activation energy for diffusion, R is the universal gas constant, and T is the absolute temperature in Kelvin. The activation energy of the increased BFR can be calculated by determining the natural logarithm of Equation (3). The diffusion coefficient can then be expressed as Equation (4):

$$\ln D = \ln D_0 - \frac{Q}{R}\left(\frac{1}{T}\right) \tag{4}$$

The calculated activation energies (Q) are shown in Figure 7. The activation energy of the SP solder ribbon joint in the PV module was 113.4 KJ/mol, and that of the SAP solder joint was 39.5 KJ/mol. We can attribute the broken MFs activation energy to the increasing BFR activation energy, as both the broken MFs and BFR increase have the same defect factor from the thermal shock test. In this study, the BFR was deactivated in the −40–65 °C test condition, and the BFR increase was activated in the −40–85 °C test condition. Finally, the greatest increase in BFR was confirmed under the −40–105 °C

test condition in the SP solder joint. The BFR increased for all test conditions in the SAP solder. In conclusion, we confirmed that broken MFs were activated at the mid-temperature range of 85 °C in the SP solder joint, whereas the broken MFs of the SAP solder joints were activated at low-temperatures around 65 °C. The SAP solder joint had a lower thermal stress and temperature resistance than the SP solder joint, and we confirmed that the broken MFs activation energy was lower than that of the SP solder joints.

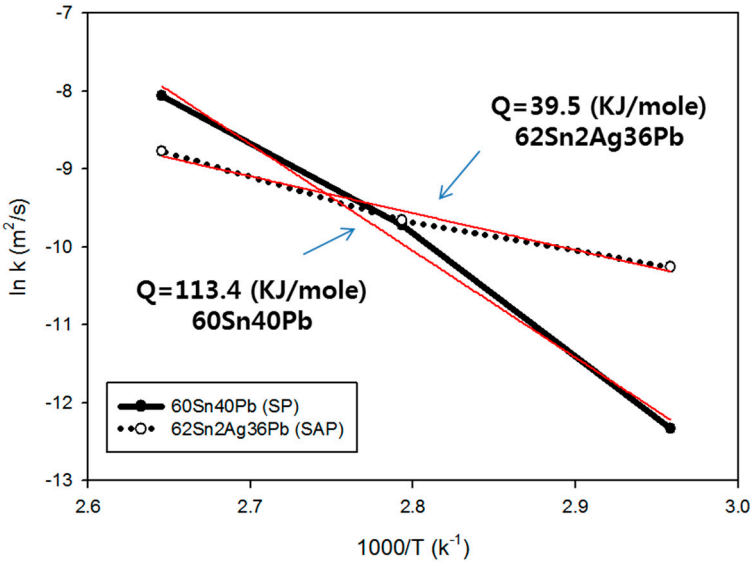

Figure 7. Activation energies of broken MFs.

We observed changes in the solder structure of PV ribbon solder joints via cross-sectional images and polishing, as shown in Figures 8 and 9, in order to analyze various broken MFs tendencies according to solder composition. From the cross-sectional images, the lead (Pb) structure in the SP solder joint was confirmed to be spherical, as shown in Figure 8. Before the thermal shock test, the average Pb grain diameter was confirmed as 4 μm. The average Pb grain size grew according to the test conditions until reaching 8 μm (−40–65 °C), 7 μm (−40–85 °C), and 16 μm (−40–105 °C). Generally, Pb grain coarsening was observed in the solder joint, which is due to the aging effects at high temperatures [20,21]. This phenomenon also influences degradation characteristics in the solder joint.

The Pb structure in the SAP solder joint was confirmed as a flake structure, as shown in Figure 9. Before the test, the average Pb grain size was confirmed as 3 μm. The average Pb grain size grew according to test conditions until reaching 4 μm (−40–65 °C), 6 μm (−40–85 °C), and 8 μm (−40–105 °C). The gap in grain size growth rate between the SP and SAP solders was influenced by the addition of Ag. When the thermal shock tests were performed on the SP and SAP solder joints, the added Ag and Tin (Sn) formed Ag_3Sn at high-temperatures in the solder joint and mitigated the Pb grain coarsening and grain boundary diffusion [22]. In addition, the added Ag suppressed the Pb grain coarsening and improved the solder properties due to the resulting combination as a solid solution state in the solder [23]. Son reported on the Ag additive effect in solders, which had similar effects to those of our study with 1−3 Ag wt %; however, the suppression of Pb grain coarsening was inefficient at proportions greater than 3 Ag wt % [24].

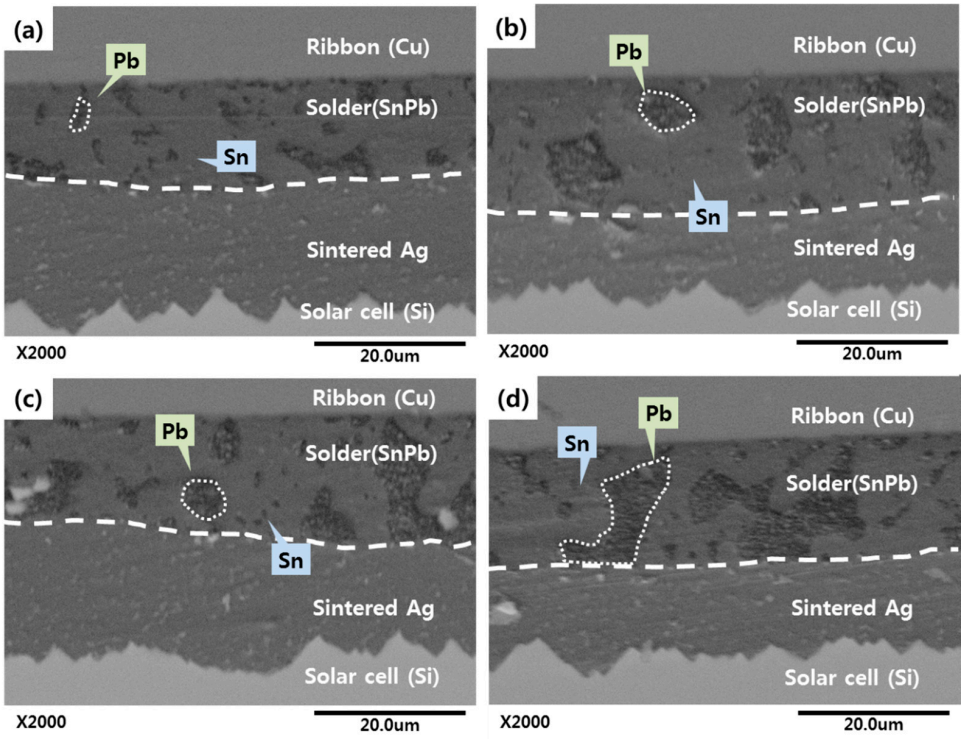

Figure 8. Pb grain size in the SP solder. (**a**) Before the test; (**b**) after 700 cycles (−40–65 °C); (**c**) after 700 cycles (−40–85 °C); and (**d**) after 700 cycles (−40–105 °C).

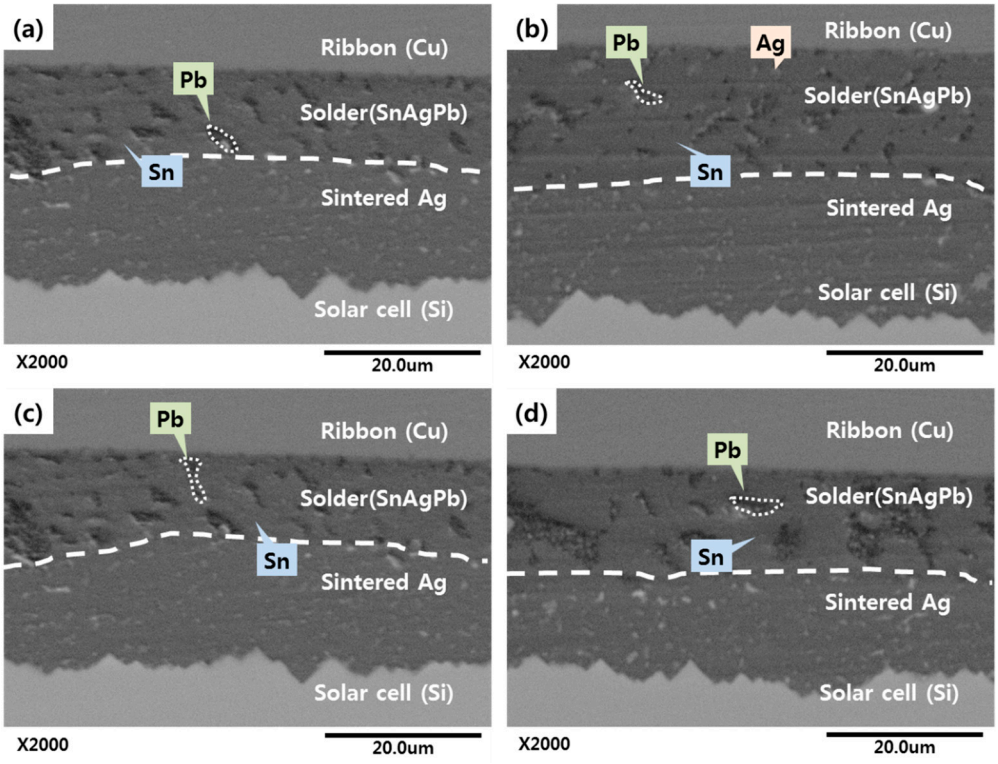

Figure 9. Pb grain size in the SnAgPb solder. (**a**) Before the test; (**b**) after 700 cycles (−40–65 °C); (**c**) after 700 cycles (−40–85 °C); and (**d**) after 700 cycles (−40–105 °C).

In this study, the broken MFs activation energies were calculated as 39.5 KJ/mol in the SAP solder joint and 113.4 KJ/mol in the SP solder joint. The SAP solder joint activation energy was lower than that of the SP solder joint due to the activation of broken MFs for all test conditions in the SAP solder joint. This indicates that the SAP solder joint initially had a low resistance to thermal stress. We analyzed the thermal-resistance gap according to the solder composition in relationship to variations in the solder structure. Before the thermal shock test, Pb grains in the SP solder joint exhibited a confirmed spherical structure, whereas Pb grains in the SAP solder joint exhibited flake structures, as shown in Figures 8a and 9a, respectively. Generally, spherical structures have superior properties such as ductility and toughness over flake structures. Therefore, we can conclude that the SP solder joint has better thermal resistance at the initial thermal shock test until the 200th cycle. Similarly, the activation energy gap can be explained according to the solder composition. In addition, we confirmed that the SAP solder joint broken MFs did not increase and actually exhibited saturation tendencies after 200 cycles under all conditions, whereas the SP solder joint broken MFs accelerated as the test progressed. This is a result of the additive effect of Ag in the solder joints. The added Ag blocked Pb grain coarsening in the SAP solder, whereas the Pb grain in the SP solder joint consistently grew during the thermal shock test. Eventually, the SP solder joint becomes brittle and weak under thermal stress due to the coarsened Pb grain as the test progresses.

4. Conclusions

In this study, we performed thermal shock tests to analyze the degradation of ribbon joint characteristics in PV module solder joints using 60Sn40Pb (SP) and 62Sn2Ag36Pb (SAP). The thermal shock tests were performed under three conditions, −40–65 °C, −40–85 °C, and −40–105 °C. The results were analyzed via EL and cross-sectional images. Following testing, broken metal fingers (MFs) appeared as dark rectangular (DR) regions in the EL images near the ribbon joints. We calculated the broken finger ratio (BFR) from the broken MFs in order to quantify the damage, where the BFR is the proportion of DRs of the entire PV module in the EL images. The broken MFs were intensively destroyed near the ribbon solder joints. This could be because the damage of the solder joint is correlated with the broken MFs. Thus, the broken MFs were calculated to the activation energy in order to appearance quantitatively the thermal degradation of ribbon solder joints. We also evaluated the stability of the PV ribbon solder joint according to additive Ag in the solder using the thermal shock test. The main conclusions of our study can be summarized as follows.

(1) The SP solder joint broken MFs were inactivated at the low-temperature condition, −40–65 °C, and were accelerated at high-temperature conditions and increasing ΔT; the broken MFs activation energy was 113.4 KJ/mol. The SAP solder joint broken MFs were activated under all test conditions, and the activation energy was 39.5 KJ/mol.

(2) Pb grains in the SP solder joint exhibited a verified spherical structure, and Pb grain coarsening occurred as the thermal shock test progressed. The average initial Pb grain size was measured as 4 μm and grew according to the test conditions until reaching 8 μm (−40–65 °C), 7 μm (−40–85 °C), and 16 μm (−40–105 °C) after the 700th thermal shock cycle. The Pb grain in the SAP solder joint exhibited a confirmed flake structure, and the average initial Pb grain size was measured as 3 μm, reaching 4 μm (−40–65 °C), 6 μm (−40–85 °C), and 8 μm (−40–105 °C) during the thermal shock test.

(3) The SAP solder joint was confirmed as the weakest point for thermal-stress at initial thermal shock testing (until the 200th cycle); this is because the SAP solder joint has lower ductility and toughness than the SP solder joint according to comparison results of the grain structure. As the thermal shock test progressed, the Pb grain growth increased in the SP solder joint, whereas the added Ag suppressed Pb coarsening in the SAP solder. As a result, the SP solder joint exhibited decreasing ductility, and the SAP solder joint broken MFs were saturated after the 200th cycle.

(4) In the future, when PV ribbons are tabbed on ribbon joints in PV modules, additional studies are needed regarding the effects of cooling temperature and cooling time at initial conditions to

improve the thermal resistance and ductility in SAP solder ribbon joints. Further studies on controlling the grain structure and coarsening are also needed.

Author Contributions: The authors contributed equally to this work.

Conflicts of Interest: The authors declare no conflict of interest.

References

1. Jeon, Y.-J.; Kim, D.-S.; Shin, Y.-E. Study of characteristics of solar cells through thermal shock and high-temperature and high-humidity testing. *Int. J. Precis. Eng. Manuf.* **2014**, *15*, 355–360. [CrossRef]
2. Zhu, H.; Li, X.; Sun, Q.; Nie, L.; Yao, J.; Zhao, G. A power prediction method for photovoltaic power plant based on wavelet decomposition and artificial neural networks. *Energies* **2016**, *9*, 11. [CrossRef]
3. Leccisi, E.; Raugei, M.; Fthenakis, V. The Energy and environmental performance of ground-mounted photovoltaic systems—A timely update. *Energies* **2016**, *9*, 622. [CrossRef]
4. Müller, A.; Ghosha, M.; Sonnenscheinb, R.; Woditscha, P. Silicon for photovoltaic applications. *Mater. Sci. Eng. B* **2006**, *134*, 257–262. [CrossRef]
5. Green, M.A. The path to 25% silicon solar cell efficiency: History of silicon cell evolution. *Prog. Photovolt. Res. Appl.* **2009**, *17*, 183–189. [CrossRef]
6. Collins, E.; Dvorack, M.; Mahn, J.; Mundt, M.; Quintana, M. Reliability and availability analysis of a fielded photovoltaic system. In Proceedings of the 2009 34th IEEE Photovoltaic Specialists Conference (PVSC), Philadelphia, PA, USA, 7–12 June 2009; pp. 002316–002321.
7. Polverini, D.; Field, M.; Dunlop, E.; Zaaiman, W. Polycrystalline silicon PV modules performance and degradation over 20 years. *Prog. Photovolt. Res. Appl.* **2013**, *21*, 1004–1015. [CrossRef]
8. Jordan, D.; Kurtz, S.R. Photovoltaic degradation rates—An analytical review. *Prog. Photovolt. Res. Appl.* **2013**, *21*, 12–29. [CrossRef]
9. Herrmann, W.; Bogdanski, N.; Reil, F.; Köhl, M.; Weiss, K.-A.; Assmus, M.; Heck, M. PV module degradation caused by thermomechanical stress: Real impacts of outdoor weathering versus accelerated testing in the laboratory. In *Reliability of Photovoltaic Cells, Modules, Components, and Systems III*; SPIE: Bellingham, WA, USA; pp. 77730I–77730I-9.
10. Yang, T.L.; Huang, K.Y.; Yang, S.; Hsieh, H.H.; Kao, C.R. Growth kinetics of Ag_3Sn in silicon solar cells with a sintered Ag metallization layer. *Sol. Energy Mater. Sol. Cells* **2014**, *123*, 139–143. [CrossRef]
11. Kirchartz, T.; Helbig, A.; Reetz, W.; Reuter, M.; Werner, J.H.; Rau, U. Reciprocity between electroluminescence and quantum efficiency used for the characterization of silicon solar cells. *Prog. Photovolt. Res. Appl.* **2009**, *17*, 394–402. [CrossRef]
12. Munoz, M.A.; Alonso-Garcíab, M.C.; Velab, N.; Chenlob, F. Early degradation of silicon PV modules and guaranty conditions. *Sol. Energy* **2011**, *85*, 2264–2274. [CrossRef]
13. Tsai, D.-M.; Wu, S.-C.; Li, W.-C. Defect detection of solar cells in electroluminescence images using Fourier image reconstruction. *Sol. Energy Mater. Sol. Cells* **2012**, *99*, 250–262. [CrossRef]
14. Bokalič, M.; Topič, M. Luminescence imaging techniques for solar cell local efficiency mapping. In Proceedings of the 47th International Conference on Microelectronics, Devices and Materials and the Workshop on Organic Semiconductors, Technologies and Devices (MIDEM 2011), Ajdovščina, Slovenia, 28–30 September 2011; pp. 229–234.
15. Bokalič, M.; Topič, M. Module Level Electroluminescence Imaging. In *Spatially Resolved Characterization in Thin-Film Photovoltaics*; Springer: Berlin, Germany, 2015; pp. 81–95.
16. Lin, K.; Leea, Y.-H.; Huanga, W.-Y.; Chena, G.; Kuoa, Y.-W.; Wanga, L.-K.; Yangb, S.-Y. Detection of soldering induced damages on crystalline silicon solar modules fabricated by hot-air soldering method. *Renew. Energy* **2015**, *83*, 749–758. [CrossRef]
17. Chaturvedi, P.; Hoex, B.; Walsh, T.M. Broken metal fingers in silicon wafer solar cells and PV modules. *Sol. Energy Mater. Sol. Cells* **2013**, *108*, 78–81. [CrossRef]
18. Mookam, N.; Kanlayasiri, K. Evolution of intermetallic compounds between Sn-0.3 Ag-0.7 Cu low-silver lead-free solder and Cu substrate during thermal aging. *J. Mater. Sci. Technol.* **2012**, *28*, 53–59. [CrossRef]
19. Nesswetter, H.; Lugli, P.; Bett, A.W.; Zimmermann, C.G. Electroluminescence and photoluminescence characterization of multijunction solar cells. *IEEE J. Photovolt.* **2013**, *3*, 353–358. [CrossRef]

20. Hsieh, H.-H.; Lin, F.-M.; Yeh, F.-Y.; Lin, M.-H. The effects of temperature and solders on the wettability between ribbon and solar cell. *Sol. Energy Mater. Sol. Cells* **2009**, *93*, 864–868. [CrossRef]
21. Ubachs, R.L.J.M.; Schreurs, P.J.G.; Geers, M.G.D. Microstructural behaviour of solder alloys. In Proceedings of the IEEE 5th International Conference on Thermal and Mechanical Simulation and Experiments in Microelectronics and Microsystems (EuroSimE 2004), Brussels, Belgium, 10–12 May 2004; pp. 543–547.
22. Frear, D.R. Microstructural evolution during thermomechanical fatigue of 62Sn-36Pb-2Ag and 60Sn-40Pb solder joints. *IEEE Trans. Compon. Hybrids Manuf. Technol.* **1990**, *13*, 718–726. [CrossRef]
23. Charles, H.K.; Romenesko, B.M. The reflow attachment and reliability testing of ceramic chip carriers. In Proceedings of the IEEE 19th Annual Reliability Physics Symposium, Orlando, FL, USA, 7–9 April 1981; pp. 93–103.
24. Son, Y.-S.; Cho, T.-S. Effects of Ag on the Characteristics of Sn-Pb-Ag Solder for Photovoltaic Ribbon. *J. Korean Inst. Electr. Electron. Mater. Eng.* **2015**, *28*, 332–337. [CrossRef]